PHYSICS

Quantum sensing of radio-frequency signal with NV centers in SiC

Zhengzhi Jiang[1,2], Hongbing Cai[3,4], Robert Cernansky[3,5], Xiaogang Liu[1,2,6]*, Weibo Gao[3,4,7]*

Copyright © 2023 The Authors, some rights reserved; exclusive licensee American Association for the Advancement of Science. No claim to original U.S. Government Works. Distributed under a Creative Commons Attribution NonCommercial License 4.0 (CC BY-NC).

Silicon carbide is an emerging platform for quantum technologies that provides wafer scale and low-cost industrial fabrication. The material also hosts high-quality defects with long coherence times that can be used for quantum computation and sensing applications. Using an ensemble of nitrogen-vacancy centers and an XY8-2 correlation spectroscopy approach, we demonstrate a room-temperature quantum sensing of an artificial AC field centered at ~900 kHz with a spectral resolution of 10 kHz. Implementing the synchronized readout technique, we further extend the frequency resolution of our sensor to 0.01 kHz. These results pave the first steps for silicon carbide quantum sensors toward low-cost nuclear magnetic resonance spectrometers with a wide range of practical applications in medical, chemical, and biological analysis.

INTRODUCTION

Solid-state spin defects are promising platforms for quantum applications such as quantum computing, sensing, and communication (*1*–*4*). These spin defects or color centers have spin ground states that can be optically polarized and detected due to spin-dependent intersystem crossing (*5*). Among them, negatively charged nitrogen-vacancy (NV) centers in diamond have shown prominent spin properties and attracted extensive studies (*6*–*8*). NV in diamond has been used to detect individual proteins and image magnetic domains in van der Waals materials (*9*, *10*). Furthermore, it has demonstrated high-resolution nuclear magnetic resonance spectroscopy of biological structures at both nano- and micrometer spatial domains using a synchronized readout technique (*11*–*13*). This powerful approach enables to extend the spectral resolution of quantum sensors beyond its physical limits given either by the relaxation (T_1) or decoherence time (T_2).

Although NV centers in diamond have shown remarkable spin properties, diamond as a host material is not compatible with conventional electronic circuits (*14*). By comparison, silicon carbide (SiC) is a technology-friendly material with a large-scale production capacity and mature doping techniques (*5*). Several kinds of color centers in SiC have been identified and proven promising for quantum applications (*15*, *16*). NV centers in SiC are reported to show spin properties similar to NV in diamonds (*17*). Moreover, the excitation and emission wavelengths for NV centers in SiC are in the near-infrared range, which is preferred for bioimaging (*18*, *19*). Recently, coherent control of NV ensembles in 4H SiC at room temperature was reported (*20*). However, the short decoherence time T_2 caused by the noise of the nuclear spin bath and other paramagnetic species limits their further applications.

Here, we extend T_2 of NV in SiC up to 10 times longer than with spin echo using the dynamical decoupling technique also known as the XY8-N pulse sequence. As a result, we perform radio-frequency (RF) signal detection at ~900 kHz with a resolution of 10 kHz using the correlation spectroscopy approach. This spectral resolution is limited by the T_1 time of the SiC NV center. The experiment scheme is shown in Fig. 1A. To extend the spectral resolution of our sensor, we use the synchronized readout technique to further improve the resolution by 1000 times down to 0.01 kHz. These results show a great promise of SiC defects to be used as emerging quantum sensors for future practical applications.

RESULTS AND DISCUSSION

Structure and low-temperature spectrum

The investigated sample contains a high concentration of NV centers created by irradiating N-doped 4H SiC (Wolfspeed) with 12-MeV protons and subsequent annealing at a high temperature (900°C) for 12 hours (*21*). The NV center in 4H SiC consists of a nitrogen atom instead of a carbon atom and an adjacent silicon vacancy (*22*). Because of the two nonequivalent sites designated as "h" (quasihexagonal) and "k" (quasicubic) in 4H SiC, there are a total of four configurations (Fig. 1B). Among them, hh and kk are axial with C_{3v} symmetry. Our studies focus on the two axial NV defects. The other two basal configurations are hk and kh (*23*). Upon off-resonance excitation with a 980-nm laser at 10 K, these four types of NV centers show distinct zero-phonon lines (ZPLs) (Fig. 1C). Each NV peak is labeled according to its NV configuration (*21*). The weak ZPL and their phonon sideband signals in the range from 1000 to 1150 nm indicate the coexistence of some divacancies. The ZPL of divacancy defects (PL4 and PL5) are labeled. The peak at approximately 1173 nm is the ZPL of Unknown Defect-1, which arises from tungsten impurities in substitutional positions (labeled as W_{Si} in Fig. 1C) (*24*, *25*). The presence of tungsten impurities could be due to annealing in the furnace.

All spin manipulation experiments were performed using a homemade confocal microscope (see details in the Supplementary

[1]Joint School of National University of Singapore and Tianjin University, International Campus of Tianjin University, Binhai New City, Fuzhou 350207, P. R. China. [2]Department of Chemistry, National University of Singapore, Singapore 117543, Singapore. [3]Division of Physics and Applied Physics, School of Physical and Mathematical Sciences, Nanyang Technological University, Singapore 637371, Singapore. [4]The Photonics Institute and Centre for Disruptive Photonic Technologies, Nanyang Technological University, Singapore 637371, Singapore. [5]Institute for Quantum Optics and IQST, Ulm University, Albert-Einstein-Allee 11, Ulm D-89081, Germany. [6]Institute of Materials Research and Engineering, Agency for Science, Technology and Research, Singapore 138634, Singapore. [7]Centre for Quantum Technologies, National University of Singapore, Singapore 117543, Singapore.
*Corresponding author. Email: chmlx@nus.edu.sg (X.L.); wbgao@ntu.edu.sg (W.G.)

Downloaded from https://www.science.org on May 21, 2023

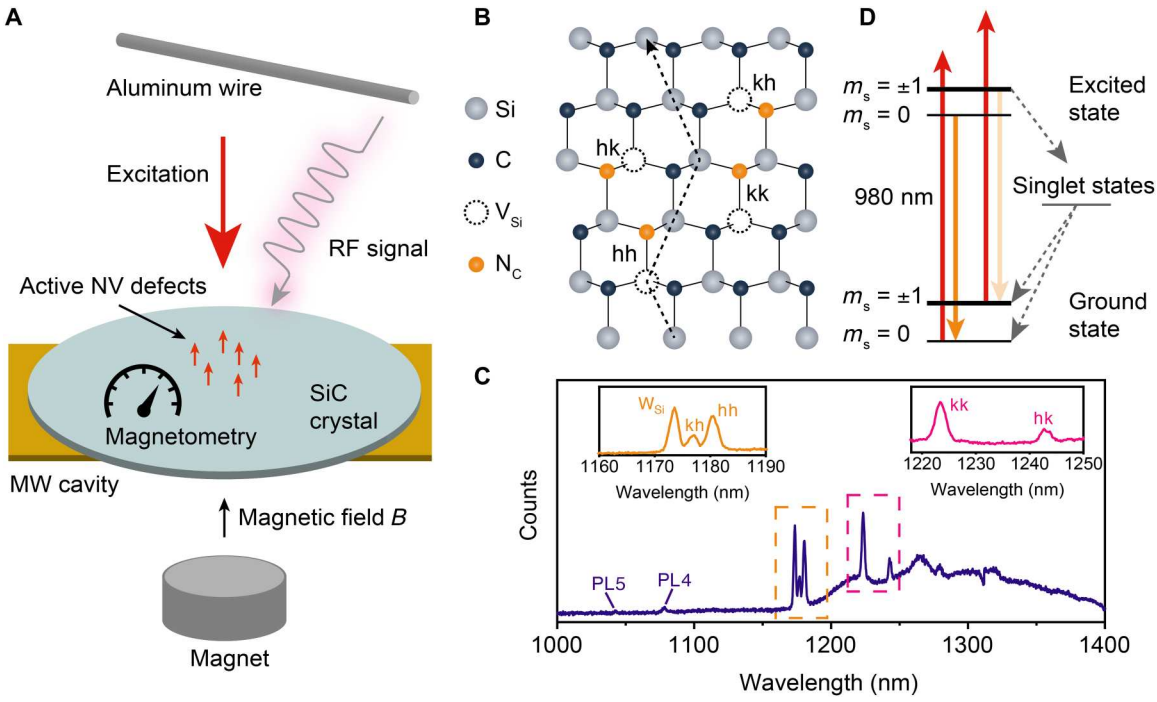

Fig. 1. Experiment scheme and different structures. (**A**) Scheme of the RF quantum sensing. (**B**) Four configurations of NV centers in 4H SiC. (**C**) Photoluminescence spectrum obtained at 10 K with 980-nm off-resonance excitation. Zero-phonon lines (ZPLs) of different NV configurations are labeled in the insets. VV defects are also labeled (PL5 and PL4). W_{si} is UD-1 defect, which arises from tungsten impurities in substitutional positions. (**D**) Simplified energy-level diagram of an NV center in 4H SiC. A 980-nm laser (red arrows) can be used to optically excite the NV center from spin-triplet ground state to spin-triplet excited state with spin conserved. From the excited state manifold, the NV can decay radiatively and emit a red-shifted photon (orange arrows). The m_s = ±1 states are dimmer than the m_s = 0 state due to the spin-dependent intersystem crossing (dashed gray arrows).

Materials). A 50×/0.65 infrared (IR) objective is used to focus the excitation laser on the sample and collect fluorescence. A 980-nm laser with an integrated modulator provides off-resonance excitation for the sample. After passing the signal through a 1250-nm-long pass filter, the PL signal is coupled into a multimode fiber and guided to a variable-gain photoreceiver. The microwave is generated by an RF signal generator and gated by an RF switch. After amplification by a high-power amplifier, the microwave is applied to the sample either via a self-designed antenna or a golden omega hoop (d = 100 μm) on the sample surface.

ODMR and coherent manipulation

Identification of the axial NV can be done by observing the optically detected magnetic resonance (ODMR) while varying the axial magnetic field strength. A simplified energy-level diagram is shown in Fig. 1D. The spin-dependent intersystem crossing contributes to the spin polarization and the ODMR contrast. The electronic ground state spin Hamiltonian of NV in 4H SiC is

$$H = D[S_z^2 - S(S+1)/3] + E(S_x^2 - S_y^2) + g\mu_B B S_z$$

where D and E are axial and transversal components of the zero-field splitting parameter, S is the total spin quantum number, and $S_{x,y,z}$ are the Pauli spin matrices. The last term describes the Zeeman effect where g, μ_B, and B are the electron g factor, the Bohr magneton, and the static magnetic field, respectively (*20*). For axial NV, E has been reported to be 0, and the last term provides a linear relationship between its ODMR and magnetic field strength (*21*). By scanning the value of the axial magnetic field, we find two sets of ODMR signals with linear behavior, as guided by the gray and red dashed lines in Fig. 2A.

To further identify them, the ODMR at 0 G was measured (Fig. 2B). By fitting the zero-field data with multiple Lorentz peaks, we obtain D_{red} = 1319.75 ± 0.07 MHz, E_{red} = 0 MHz, D_{gray} = 1276 ±0.99 MHz, and E_{gray} = 6.65 ± 0.99 MHz. The fitted D_{red} and D_{gray} agree well with previously reported ZFS values of hh and kk NV in 4H SiC, respectively (*14*, *20*). Here, we assign the red set and gray set ODMR to signals from hh and kk NV, respectively. The small finite value of E_{gray} warrants further measurements to fully understand the origin of the nonzero E value for the kk NV center. We also note that the hyperfine splitting caused by adjacent nitrogen atoms is difficult to resolve because of inhomogeneous broadening in our sample. For the other three pairs of NV centers exhibiting basal behaviors with one pair appearing faint in the middle, we tentatively identified them as basal NV centers. These basal NV centers are oriented in three different directions, which explain the observation of three pairs.

To get an upper limit of our coherence enhancement, we study the longitudinal relaxation time of hh NV defects (*3*). The longitudinal relaxation time imposes an upper limit on decoherence time $T_{2(max)} = 2T_1$. Focusing on the transition between m_s = 0 and m_s = +1 of hh NV, T_1 and Rabi measurements are performed at 65 G. Coherent Rabi oscillation is shown in Fig. 2C with a Rabi frequency of 3.73 MHz. T_1 is fitted to be 100 ± 1.6 μs using a single exponential decay function (Fig. 2D).

Downloaded from https://www.science.org on May 21, 2023

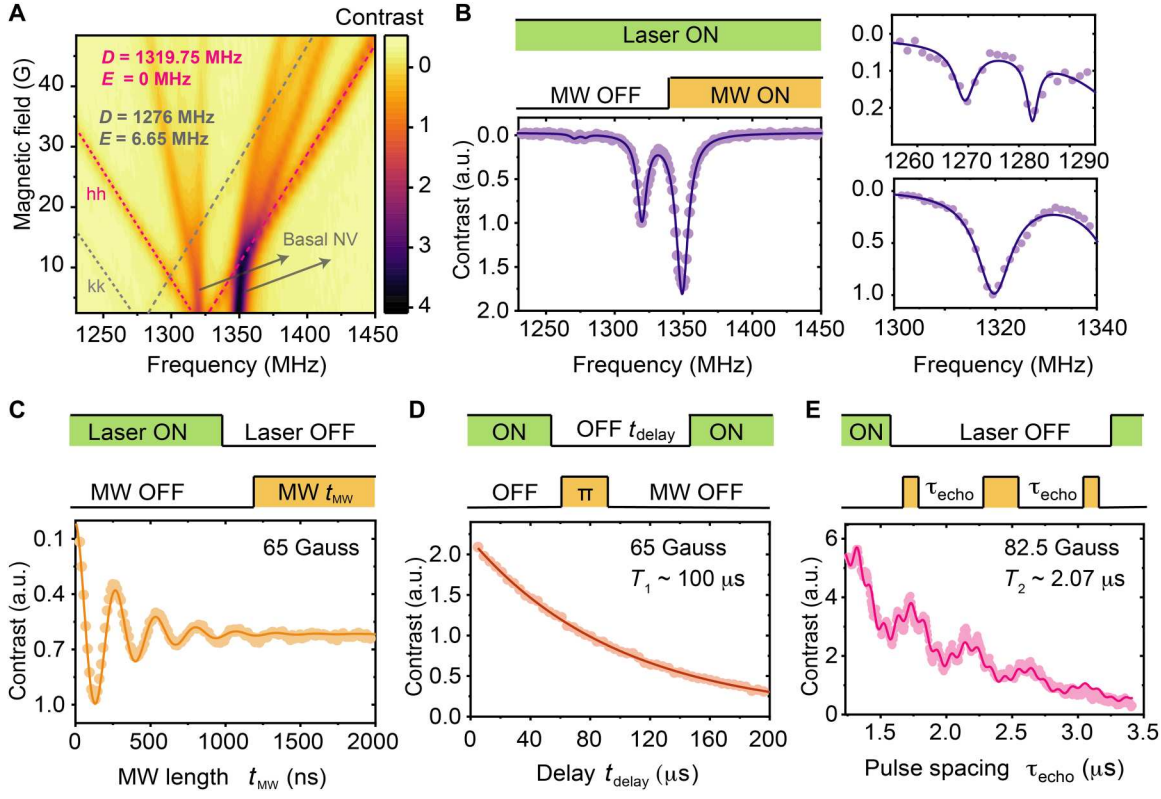

Fig. 2. Measurements of spin properties. (**A**) Magnetic field–dependent Continuous-Wave–optically detected magnetic resonance (ODMR). The direction of the magnetic field is along the *c* axis of SiC. Gray and red dashed lines indicate the ODMR of kk and hh NV centers, respectively. (**B**) Left: Full CW-ODMR spectrum measured at 0 G. Right: Zoomed-in zero-field ODMR of kk (top) and hh (bottom) NV centers. (**C**) Rabi measured at 65 G. The solid curve represents a theoretical fit with a damped sine function. (**D**) T_1 of the hh NV center at 65 G. It is fitted (solid curve) to a single exponential decay, obtaining $T_1 = 100 \pm 1.6$ μs. (**E**) Spin echo spectroscopy measured at 82.5 G. Experimental data are fitted to $\exp(-2\tau_{echo}/T_2)[a - b \sin^2(\omega_1\tau_{echo}/2) - c \sin^2(\omega_2\tau_{echo}/2)]$, yielding the $\omega_1 \sim 2\pi$ 9.8 MHz, $\omega_2 \sim 2\pi$ 2.3 MHz, and $T_2 = 2.073 \pm 0.017$ μs. Top panels show their corresponding pulse sequences. a.u., arbitrary units.

The spin echo spectroscopy is found to be modulated at 82.5 G, as shown in Fig. 2E. The spectroscopy from 1.08 μs onward can be well fitted with expected functional form $\exp(-2\tau_{echo}/T_2)[a - b \sin^2(\omega_1\tau_{echo}/2) - c \sin^2(\omega_2\tau_{echo}/2)]$ (*6*). Both the two frequencies (ω_1=2π 9.8 MHz and ω_2=2π 2.3 MHz) in spin echo spectroscopy exceed the bare Larmor precession rate of ^{29}Si (2π 0.07 MHz) and ^{13}C (2π 0.088 MHz) at this magnetic field. To identify them, we have varied the magnitude of the magnetic field to 52.7 G and measured spin echo data. Figure S6A shows the result. We subtracted the baseline and then applied Fourier transformation to obtain the frequency spectrum. The frequency spectrum is shown in fig. S6B. The two main frequencies are similar to those at 82.5 G. This means that they both do not depend on an external magnetic field, which is the feature of hyperfine-induced modulations (*6*). We verified that the 9.8-MHz modulation comes from the closest ^{29}Si, which has a known hyperfine coupling of 9.8 ± 0.2 MHz with PL6 (*26*). The 2.3-MHz modulation may originate from the next-closest ^{29}Si or the closest ^{13}C. Because no similar modulation is observed in the NV ensemble in diamond, we suspect that the 2.3-MHz modulation comes from the next-closest ^{29}Si, because it is more abundant than 13C. These modulations provide the possibility to make use of the fruitful nuclear environments of NV centers in SiC (*27*–*29*).

Extension of decoherence time using dynamical decoupling

The increase in coherence time can be observed directly by comparing the signal contrast as a function of interrogation time for different sequences. For all measurements, the contrasts decay with increasing interrogation time as the observed transition probability $\delta p_{obs}(t)$ decreases

$$\delta p_{obs}(t) = \delta p(t) e^{(\Gamma t)^a}$$

where t is the interrogation time, Γ is the decay rate, and a = 1, ..., 3 (*3*). The decoherence time or relaxation time $T_\chi = \Gamma^{-1}$ depends on the effects of noise and sets the maximum possible time for quantum manipulations. Considering that the bath-noise spectrum in a solid system has a soft cutoff, here, we choose XY8-N sequences (*30*). The XY8-N sequences consist of three parts (Fig. 3A). The first part is a π/2 pulse that prepares the superposition state after initialization. The second part is an N set of eight π pulses with alternating phases: x-y-x-y-y-x-y-x, which can partly compensate for pulse errors (*31*). The final one is another π/2 pulse, which is used to project the output from the superposition state to a measurable state. In experiments, we measure the outputs of two cascade XY8-N measurements with different phases of the final π/2 pulse. The first XY8-N measurement has $\pi/2_x$ as the final pulse while the following pulse sequence has $\pi/2_{-x}$. The first and second XY8-N

Downloaded from https://www.science.org on May 21, 2023

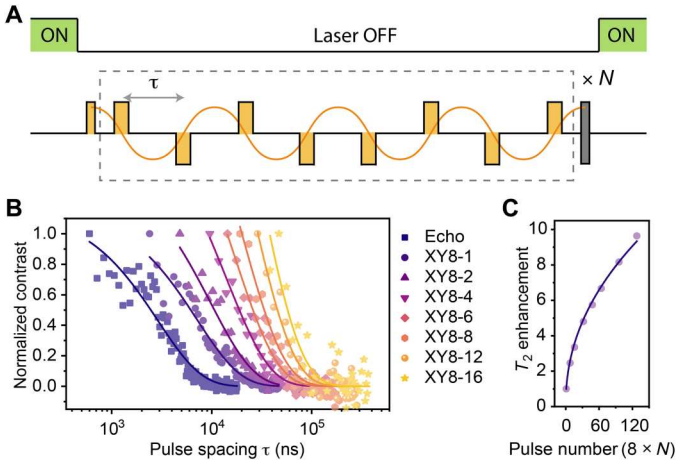

Fig. 3. Dynamical decoupling. (**A**) Pulse sequence of the XY8-N measurement. Top part represents laser state. The bottom part displays the MW and RF signals. The orange wavy line represents an RF signal. Thin blocks and thick blocks are π/2 pulses and π pulses, respectively. The rotation axes of the XY8-N pulses are indicated as different directions (up for *x* and down for *y*). The final gray thin pulse is $(\pi/2)_{-x}$ for SIG_1 and $(\pi/2)_x$ for SIG_2. The contrast is calculated as $(SIG_1 - SIG_2)/(SIG_1 + SIG_2)$. (**B**) Normalized decay signals from spin echo and XY8-N measurements. The solid curves represent fits with a single exponential decay. (**C**) Enhancement of the coherence time (T/T_{echo}) as a function of the number of π pulses. The enhancement is equal to $(8 \times N)^{0.46\pm0.003}$.

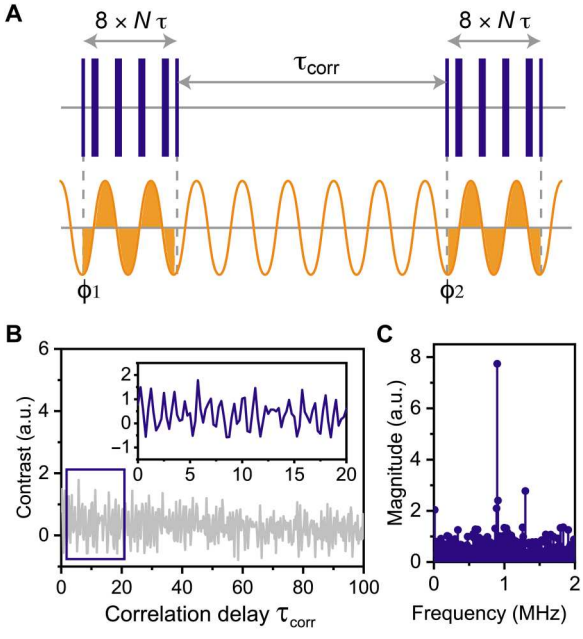

Fig. 4. Quantum sensing with XY8-2 correlation spectroscopy. (**A**) Diagram of XY8-N correlation spectroscopy. The purple part is the microwave pulse sequence. The yellow part is the AC signal. τ is fixed at half of the AC signal period, and τ_{corr} is swept to correlate ϕ_1 and ϕ_2 phases. (**B**) Data of the XY8-2 correlation spectroscopy and (**C**) its Fourier-transformed results. The peak frequency is 898 kHz.

measurements produce SIG_1 and SIG_2 outputs, respectively. To reduce noise from laser fluctuations and microwave errors, we calculate the contrast using $(SIG_1 - SIG_2)/(SIG_1 + SIG_2)$ (*32*, *33*).

These sequences act as a filter with a bandwidth $\Delta f \approx 1/(8 \times N \times \tau)$, where τ is the spacing between two π pulses. They can decouple the target spins from magnetic fluctuations that are not resonant with their center frequencies $f_k = k/(2\tau)$, where k is an integer. For $k > 1$, the higher harmonics at f_k are suppressed. With a larger number of π pulses, XY8-N sequences have a narrower bandwidth and thus provide better isolation of the target spins from noise. We use spin echo and XY8-N pulse sequences to measure and compare the achievable decoherence times of an ensemble of NV centers in SiC (Fig. 3B). By normalizing the contrast, we find that the decoherence time measured with XY8-16 is extended to 28.1 μs, which is one order of magnitude longer than that measured with the spin echo. Besides hh NV, we find that the decoherence time of kk NV can also be extended using dynamic decoupling sequences (see the Supplementary Materials).

To investigate how the decoherence time scales with the number of pi pulses, we fit the enhancement factor T/T_{echo} as a function of the number of π pulses $8 \times N$ (inset of Fig. 3B), where T_{echo} is the decoherence time measured by spin echo. The fitting result shows that the decoherence time scales with $(8 \times N)^{0.46\pm0.003}$, which is below the theoretical prediction $T/T_{echo} \propto (8 \times N)^{2/3}$ for noise sources with correlation time $\tau_c \gg T_2$ (*30*, *34*). We do not expect to observe the $N^{2/3}$ scaling in our experimental conditions, as we are not in the regime where the bath correlation time is much greater than the NV coherence time. Moreover, imperfections of our control pulses and a small misalignment of the magnetic field can also contribute to the deviation (*35*). The extended T_2 is comparable to T_1 but still significantly below the theoretical T_1 limit, which may be influenced by the presence of electrical noise from the bulk (*36*, *37*). Further investigation is required to comprehensively understand the spin baths in SiC.

Quantum sensing of RF signal with XY8-2 correlation spectroscopy

To detect the RF signal with a T_1 limited spectral resolution, we performed correlation spectroscopy to sense an RF placed over the sample with a wire (*38*, *39*). The correlation spectroscopy pulse sequence consists of two XY8-N or spin echo sequences with τ fixed at half of the RF signal period (Fig. 4A). Phases accumulated in the first and second interrogations are labeled as ϕ_1 and ϕ_2, respectively. When the spacing between the two sequences, t_{corr}, is swept, ϕ_1 and ϕ_2 become correlated. As a result, the final fluorescence intensity oscillates. By performing fast Fourier transform (FFT) for correlation spectroscopy, one can extract the frequency of the RF signal. The FFT result of the measured XY8-2 correlation spectroscopy is shown in Fig. 4B. The frequency of the peak is 898 kHz with a resolution of 10 kHz. The peak frequency is close to the 900 kHz of the applied AC signal. The spectral resolution is limited by the Fourier transform of the longest t_{corr} in our experiment, which is 100 μs. For longer t_{corr}, higher resolution can be reached and is ultimately limited by the relaxation time T_1, which is 100 μs.

To show the advantages of the extended decoherence time, we compare the signal-to-noise ratio (SNR) between spin echo and XY8-2 correlation spectroscopy. The SNR of XY8-2 correlation spectroscopy is calculated to be 20.1 using the method in (*40*). For comparison, the SNR of spin echo correlation spectroscopy

Downloaded from https://www.science.org on May 21, 2023

with the same measurement time is 13.39 (see the Supplementary Materials). By minimizing the phase error in control pulses and choosing an RF signal with an even smaller amplitude, a greater enhancement of SNR is expected to be achieved.

Quantum sensing with high spectral resolution using synchronized readout

Last, to demonstrate RF detection with the Fourier-limited high spectral resolution, we implement synchronized readout with the hh NV (*11*, *12*). The sequence of synchronized readout is shown in Fig. 5A. It performs continuous sampling (purple) of the target signal (yellow) and then provides frequency information from the undersampled outputs (red). The undersampled outputs can be decoded by analyzing the interaction of a NV center with the AC signal of the form $H(t) = \kappa\sigma_z \sin(2\pi\nu_{AC}t + \phi)$, where κ is the interaction strength, σ_z is the Pauli matrix. ν_{AC} and ϕ are frequency and an arbitrary phase of the AC signal, respectively (*11*). After being prepared into superposition state $\frac{1}{\sqrt{2}}(|0\rangle + |-1\rangle)$, the relative phase accumulated between two of the sensor's spin levels, $|0\rangle$ and $|-1\rangle$, during an XY8-2 measurement can be expressed as $\Phi = \frac{16\kappa}{\pi\nu_{AC}}\cos(\varphi)$. Figure 5B shows two specific cases with $\phi = 0$ and $\varphi = \frac{\pi}{2}$, where the amplitudes of accumulated phase reach maximum and minimum, respectively. For successive XY8-2 measurements, the accumulated phase of nth measurement is $\Phi = \frac{16\kappa}{\pi\nu_{AC}}\cos[2\pi\delta(T_n) + \varphi]$, where $T_n = nT_L$ and $\delta = \nu_{AC} - \nu_{LO}$. T_L is the delay between the start of two consecutive XY8-2 measurements. ν_{LO} is the central frequency of synchronized readout protocol, which is defined as $\nu_{LO} = i/T_L$, where i is an integer number. The range of AC signal frequencies ν_{AC} that can be detected without aliasing is given by $\nu_{LO} \pm 1/(2T_L)$. Choosing appropriate i and T_L makes the output fluorescence oscillates at the frequency of δ.

Here, we apply an RF with 899.28 kHz and set the delay between two consecutive XY8-2 measurements T_L to be 33638 ns. Choosing $i = 30$ gives a central frequency $\nu_{LO} = \frac{i}{T_L} = 891.85$ kHz. We show the readout data in Fig. 5C. After performing a Fourier transform of the output, we determined that the detuning frequency δ is 7.43 kHz with a resolution of 0.01 kHz, as evidenced by the peak in Fig. 5D. The measured RF is then calculated to be $\nu_{AC} = \nu_{LO} + \delta = 899.28$ kHz. Attributing to its independence of quantum lifetime, the synchronized readout can reach a high spectral resolution. For longer measurement time, even higher spectral resolution can be achieved, and the main limitations are the stability of the local oscillator, which determines the T_L and the Allan variance (*3*).

In conclusion, we coherently manipulated axial NV centers in 4H SiC and extended their decoherence time with dynamic decoupling at room temperature. The extension is attributed to narrower transmission bandwidth with longer dynamic decoupling sequences, and further extension is possible for samples with superior coherence properties. We also note that spin echo spectroscopy is modulated, potentially providing tools to investigate fruitful nuclear environments. The exact origin of the modulation needs further investigation. The demonstration of AC signal sensing with improved SNR and high spectral resolution warrants the potential for applications such as quantum sensing for SiC NV centers.

MATERIALS AND METHODS

A N-doped (2×10^{17}/cm^3) 4H SiC bulk was irradiated with 12-MeV protons at a dose of 10^{16}/cm^2). The irradiated sample was

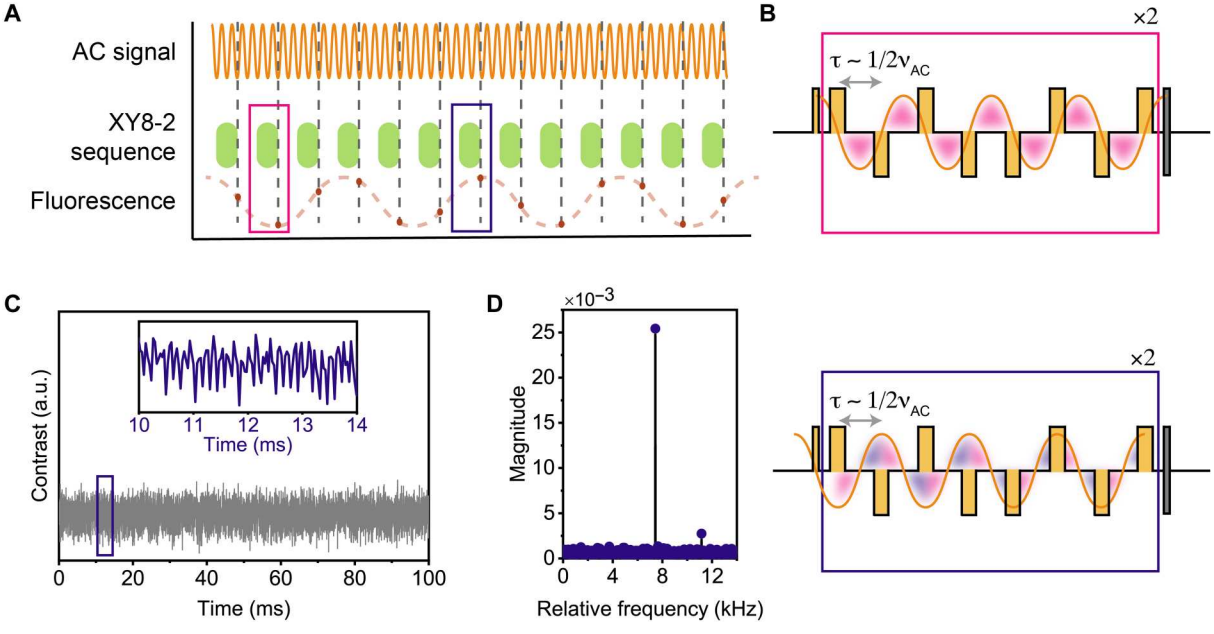

Fig. 5. Quantum sensing with synchronized readout. (**A**) Schematic of the synchronized readout measurement. AC signal is represented by a solid yellow line. Green blocks are XY8-2 measurements with a pulse spacing τ fixed at around $1/(2\nu_{AC})$. Detected fluorescence intensity (dark brown dots) depends on the accumulated phase of each XY8-2 measurement. Dashed pink and purple frames indicate XY8-2 measurements with the lowest and highest fluorescence intensities, corresponding to the maximum and minimum accumulated phases, respectively. (**B**) Phase accumulation processes during XY8-2 measurements with AC signal phase $\phi = 0$ (top) and $\varphi = \frac{\pi}{2}$ (bottom). Pink and purple areas mean positively and negatively accumulated phases, respectively. (**C**) Outputs of the synchronized readout measurement. The inset zooms in the outputs between 10 and 14 ms. (**D**) Fast Fourier transform (FFT) data of (B).

Downloaded from https://www.science.org on May 21, 2023

subsequently annealed at 900°C to create NV defects. The concentration of generated NV centers was estimated to be $10^{16}/cm^3$ (*14*, *21*). An omega hoop was deposited on the sample surface to deliver the microwaves (fig. S1).

A homebuilt confocal microscope with a 50×/0.65 IR objective was used to excite and collect fluorescence from the sample. For PL spectral measurements at low temperature, the sample was mounted on a Cryostation (MONTANA INSTRUMENTS) and cooled to 10 K. A 980-nm laser (CCS-I AeroDIODE) was used to excite the sample. Fluorescence filtered by a 1000-nm-long pass filter was coupled into a multimode fiber (50 μm) and then guided into a spectrometer (Princeton) with an InGaAs photodetector (800 to 1600 nm).

A diagram of the spin manipulation experimental setup is shown in fig. S2. Collected fluorescence was converted into electrical signals using a photodiode (FEMTO OE-200-IN) with a gain of 10^6V/W@850 nm and a bandwidth of 200 kHz. A Data Acquisition System (National Instruments USB-6343-BNC) reads the values of electrical signals (analog readout) when it received triggers from the pulse generator (Swabian Instruments Pulse Streamer 8/2). Microwave was generated by a signal generator (Stanford Research Systems SG386) and then amplified by a microwave amplifier (Minicircuits ZHL-30w-252-s+) before being delivered to the sample either via the Omega hoop or a homemade cavity with a resonant frequency of 1.39 GHz (*41*). The magnetic field was applied by either a permanent magnet or an electromagnet.

Phase controls of the microwave pulse at spin echo and XY8-N were done using the internal In-phase and Quadrature (IQ) modulator of SG386. Either +0.35-V or −0.35-V DC voltages were directed to the I and Q inputs, depending on the voltage levels controlled by the pulse generator (table S1). Details of the configuration can be found in (*32*).

Supplementary Materials

This PDF file includes:

Sections SI to SVII
Figs. S1 to S6
Table S1

REFERENCES AND NOTES

1. M. Atatüre, D. Englund, N. Vamivakas, S.-Y. Lee, J. Wrachtrup, Material platforms for spin-based photonic quantum technologies. *Nat. Rev. Mater.* **3**, 38–51 (2018).
2. L. Childress, R. Hanson, Diamond NV centers for quantum computing and quantum networks. *MRS Bull.* **38**, 134–138 (2013).
3. C. L. Degen, F. Reinhard, P. Cappellaro, Quantum sensing. *Rev. Mod. Phys.* **89**, 035002 (2017).
4. H. J. Kimble, The quantum internet. *Nature* **453**, 1023–1030 (2008).
5. D. D. Awschalom, R. Hanson, J. Wrachtrup, B. B. Zhou, Quantum technologies with optically interfaced solid-state spins. *Nat. Photonics* **12**, 516–527 (2018).
6. L. Childress, M. V. Gurudev Dutt, J. M. Taylor, A. S. Zibrov, F. Jelezko, J. Wrachtrup, P. R. Hemmer, M. D. Lukin, Coherent dynamics of coupled electron and nuclear spin qubits in diamond. *Science* **314**, 281–285 (2006).
7. F. Jelezko, T. Gaebel, I. Popa, M. Domhan, A. Gruber, J. Wrachtrup, Observation of coherent oscillation of a single nuclear spin and realization of a two-qubit conditional quantum gate. *Phys. Rev. Lett.* **93**, 130501 (2004).
8. P. London, J. Scheuer, J.-M. Cai, I. Schwarz, A. Retzker, M. B. Plenio, M. Katagiri, T. Teraji, S. Koizumi, J. Isoya, R. Fischer, L. P. McGuinness, B. Naydenov, F. Jelezko, Detecting and polarizing nuclear spins with double resonance on a single electron spin. *Phys. Rev. Lett.* **111**, 067601 (2013).
9. I. Lovchinsky, A. O. Sushkov, E. Urbach, N. P. de Leon, S. Choi, K. De Greve, R. Evans, R. Gertner, E. Bersin, C. Müller, L. McGuinness, F. Jelezko, R. L. Walsworth, H. Park, M. D. Lukin, Nuclear magnetic resonance detection and spectroscopy of single proteins using quantum logic. *Science* **351**, 836–841 (2016).
10. I. O. Robertson, C. Tan, S. C. Scholten, A. J. Healey, G. J. Abrahams, G. Zheng, A. Manchon, L. Wang, J.-P. Tetienne, Imaging current control of magnetization in Fe_3GeTe_2 with a widefield nitrogen-vacancy microscope. *2D Mater.* **10**, 015023 (2022).
11. S. Schmitt, T. Gefen, F. M. Stürner, T. Unden, G. Wolff, C. Müller, J. Scheuer, B. Naydenov, M. Markham, S. Pezzagna, J. Meijer, I. Schwarz, M. Plenio, A. Retzker, L. P. McGuinness, F. Jelezko, Submillihertz magnetic spectroscopy performed with a nanoscale quantum sensor. *Science* **356**, 832–837 (2017).
12. D. R. Glenn, D. B. Bucher, J. Lee, M. D. Lukin, H. Park, R. L. Walsworth, High-resolution magnetic resonance spectroscopy using a solid-state spin sensor. *Nature* **555**, 351–354 (2018).
13. J. M. Boss, K. S. Cujia, J. Zopes, C. L. Degen, Quantum sensing with arbitrary frequency resolution. *Science* **356**, 837–840 (2017).
14. H. J. von Bardeleben, J. L. Cantin, E. Rauls, U. Gerstmann, Identification and magneto-optical properties of the NV center in 4*H* − SiC. *Phys. Rev. B* **92**, 064104 (2015).
15. A. L. Falk, B. B. Buckley, G. Calusine, W. F. Koehl, V. V. Dobrovitski, A. Politi, C. A. Zorman, P. X.-L. Feng, D. D. Awschalom Polytype control of spin qubits in silicon carbide. *Nat. Commun.* **4**, 1819 (2013).
16. P. V. Klimov, A. L. Falk, D. J. Christle, V. V. Dobrovitski, D. D. Awschalom, Quantum entanglement at ambient conditions in a macroscopic solid-state spin ensemble. *Sci. Adv.* **1**, e1501015 (2015).
17. J. R. Weber, W. F. Koehl, J. B. Varley, A. Janotti, B. B. Buckley, C. G. Van de Walle, D. D. Awschalom, Quantum computing with defects. *Proc. Natl. Acad. Sci. U.S.A.* **107**, 8513–8518 (2010).
18. A. H. All, X. Zeng, D. B. L. Teh, Z. Yi, A. Prasad, T. Ishizuka, N. Thakor, Y. Hiromu, X. Liu, Expanding the toolbox of upconversion nanoparticles for in vivo optogenetics and neuromodulation. *Adv. Mater.* **31**, 1803474 (2019).
19. A. M. Smith, M. C. Mancini, S. Nie, Second window for in vivo imaging. *Nat. Nanotechnol.* **4**, 710–711 (2009).
20. J.-F. Wang, F.-F. Yan, Q. Li, Z.-H. Liu, H. Liu, G.-P. Guo, L.-P. Guo, X. Zhou, J.-M. Cui, J. Wang, Z.-Q. Zhou, X.-Y. Xu, J.-S. Xu, C.-F. Li, G.-C. Guo, Coherent control of nitrogen-vacancy center spins in silicon carbide at room temperature. *Phys. Rev. Lett.* **124**, 223601 (2020).
21. Z. Mu, S. A. Zargaleh, H. J. von Bardeleben, J. E. Fröch, M. Nonahal, H. Cai, X. Yang, J. Yang, X. Li, I. Aharonovich, W. Gao, Coherent manipulation with resonant excitation and single emitter creation of nitrogen vacancy centers in 4H silicon carbide. *Nano Lett.* **20**, 6142–6147 (2020).
22. Y. Zhu, B. Kovos, M. Onizhuk, D. Awschalom, G. Galli, Theoretical and experimental study of the nitrogen-vacancy center in 4H-SiC. *Phys. Rev. Materials* **5**, 074602 (2021).
23. S. A. Zargaleh, H. J. von Bardeleben, J. L. Cantin, U. Gerstmann, S. Hameau, B. Eblé, W. Gao, Electron paramagnetic resonance tagged high-resolution excitation spectroscopy of NV-centers in 4*H*-SiC. *Phys. Rev. B* **98**, 214113 (2018).
24. S. A. Zargaleh, B. Eble, S. Hameau, J.-L. Cantin, L. Legrand, M. Bernard, F. Margaillan, J.-S. Lauret, J.-F. Roch, H. J. von Bardeleben, E. Rauls, U. Gerstmann, F. Treussart, Evidence for near-infrared photoluminescence of nitrogen vacancy centers in 4*H*-SiC. *Phys. Rev. B* **94**, 060102 (2016).
25. W. F. Koehl, B. B. Buckley, F. J. Heremans, G. Calusine, D. D. Awschalom, Room temperature coherent control of defect spin qubits in silicon carbide. *Nature* **479**, 84–87 (2011).
26. J.-F. Wang, J.-M. Cui, F.-F. Yan, Q. Li, Z.-D. Cheng, Z.-H. Liu, Z.-H. Lin, J.-S. Xu, C.-F. Li, G.-C. Guo, Optimization of power broadening in optically detected magnetic resonance of defect spins in silicon carbide. *Phys. Rev. B* **101**, 064102 (2020).
27. I. Schwartz, J. Scheuer, B. Tratzmiller, S. Müller, Q. Chen, I. Dhand, Z.-Y. Wang, C. Müller, B. Naydenov, F. Jelezko, M. B. Plenio, Robust optical polarization of nuclear spin baths using Hamiltonian engineering of nitrogen-vacancy center quantum dynamics. *Sci. Adv.* **4**, eaat8978 (2018).
28. M. Pfender, N. Aslam, H. Sumiya, S. Onoda, P. Neumann, J. Isoya, C. A. Meriles, J. Wrachtrup, Nonvolatile nuclear spin memory enables sensor-unlimited nanoscale spectroscopy of small spin clusters. *Nat. Commun.* **8**, 834 (2017).
29. A. Bourassa, C. P. Anderson, K. C. Miao, M. Onizhuk, H. Ma, A. L. Crook, H. Abe, J. Ul-Hassan, T. Ohshima, N. T. Son, G. Galli, D. D. Awschalom, Entanglement and control of single nuclear spins in isotopically engineered silicon carbide. *Nat. Mater.* **19**, 1319–1325 (2020).
30. G. de Lange, Z.-H. Wang, D. Riste, V. V. Dobrovitski, R. Hanson, Universal dynamical decoupling of a single solid-state spin from a spin bath. *Science* **330**, 60–63 (2010).
31. T. Gullion, D. B. Baker, M. S. Conradi, New, compensated Carr-Purcell sequences. *J. Magn. Reson. (1969)* **89**, 479–484 (1990).

Downloaded from https://www.science.org on May 21, 2023

32. D. B. Bucher, D. P. L. Aude Craik, M. P. Backlund, M. J. Turner, O. Ben Dor, D. R. Glenn, R. L. Walsworth, Quantum diamond spectrometer for nanoscale NMR and ESR spectroscopy. *Nat. Protoc.* **14**, 2707–2747 (2019).
33. T. Wolf, P. Neumann, K. Nakamura, H. Sumiya, T. Ohshima, J. Isoya, J. Wrachtrup, Subpicotesla diamond magnetometry. *Phys. Rev. X* **5**, 041001 (2015).
34. N. Bar-Gill, L. M. Pham, C. Belthangady, D. Le Sage, P. Cappellaro, J. R. Maze, M. D. Lukin, A. Yacoby, R. Walsworth, Suppression of spin-bath dynamics for improved coherence of multi-spin-qubit systems. *Nat. Commun.* **3**, 858 (2012).
35. Y. Masuyama, K. Mizuno, H. Ozawa, H. Ishiwata, Y. Hatano, T. Ohshima, T. Iwasaki, M. Hatano, Extending coherence time of macro-scale diamond magnetometer by dynamical decoupling with coplanar waveguide resonator. *Rev. Sci. Instrum.* **89**, 125007 (2018).
36. B. A. Myers, A. Ariyaratne, A. C. B. Jayich, Double-quantum spin-relaxation limits to coherence of near-surface nitrogen-vacancy centers. *Phys. Rev. Lett.* **118**, 197201 (2017).
37. D. R. Candido, M. E. Flatté, Interplay between charge and spin noise in the near-surface theory of decoherence and relaxation of C_{3v} symmetry qutrit spin-1 centers. *Phys. Rev. X* **9**, 031052 (2023).
38. R. D. Allert, F. Bruckmaier, N. R. Neuling, F. A. Freire-Moschovitis, K. S. Liu, C. Schrepel, P. Schätzle, P. Knittel, M. Hermans, D. B. Bucher, Microfluidic quantum sensing platform for lab-on-a-chip applications. *Lab Chip* **22**, 4831–4840 (2022).
39. A. Laraoui, F. Dolde, C. Burk, F. Reinhard, J. Wrachtrup, C. A. Meriles, High-resolution correlation spectroscopy of ^{13}C spins near a nitrogen-vacancy centre in diamond. *Nat. Commun.* **4**, 1651 (2013).
40. Z. Wang, F. Kong, P. Zhao, Z. Huang, P. Yu, Y. Wang, F. Shi, J. Du, Picotesla magnetometry of microwave fields with diamond sensors. *Sci. Adv.* **8**, eabq8158 (2022).
41. K. Sasaki, Y. Monnai, S. Saijo, R. Fujita, H. Watanabe, J. Ishi-Hayase, K. M. Itoh, E. Abe, Broadband, large-area microwave antenna for optically detected magnetic resonance of nitrogen-vacancy centers in diamond. *Rev. Sci. Instrum.* **87**, 053904 (2016).

Acknowledgments

Funding: This work was supported by the Singapore Quantum engineering program (nos. NRF2021-QEP2-01-P01, NRF2021-QEP2-01-P02, NRF2021-QEP2-03-P01, NRF2021-QEP2-03-P10, and NRF2021-QEP2-03-P11), ASTAR IRG (M21K2c0116), the Singapore Ministry of Education [MOE2016-T3-1-006 (S)], and the H2020 Marie Skłodowska-Curie Actions (ID: 101018843). **Author contributions:** Z.J. carried out the measurements and performed the theoretical fittings. H.C. prepared the sample. Z.J., R.C., X.L., and W.G. analyzed the experimental data. All authors contributed to writing the manuscript. X.L. and W.G. conceived and supervised the project. **Competing interests:** The authors declare that they have no competing interests. **Data and materials availability:** All data needed to evaluate the conclusions in the paper are present in the paper and/or the Supplementary Materials.

Submitted 8 December 2022
Accepted 12 April 2023
Published 17 May 2023
10.1126/sciadv.adg2080

Downloaded from https://www.science.org on May 21, 2023

ScienceAdvances

Quantum sensing of radio-frequency signal with NV centers in SiC

Zhengzhi Jiang, Hongbing Cai, Robert Cernansky, Xiaogang Liu, and Weibo Gao

Sci. Adv., **9** (20), eadg2080.
DOI: 10.1126/sciadv.adg2080

View the article online
https://www.science.org/doi/10.1126/sciadv.adg2080
Permissions
https://www.science.org/help/reprints-and-permissions

Downloaded from https://www.science.org on May 21, 2023

Use of this article is subject to the Terms of service

Science Advances (ISSN) is published by the American Association for the Advancement of Science. 1200 New York Avenue NW, Washington, DC 20005. The title *Science Advances* is a registered trademark of AAAS.
Copyright © 2023 The Authors, some rights reserved; exclusive licensee American Association for the Advancement of Science. No claim to original U.S. Government Works. Distributed under a Creative Commons Attribution NonCommercial License 4.0 (CC BY-NC).